Available online at www.sciencedirect.com
ScienceDirect
Geochimica et Cosmochimica Acta 188 (2016) 21–34
Geochimica et Cosmochimica Acta
www.elsevier.com/locate/gca

Variable helium diffusion characteristics in fluorite

R. Wolff [a,*], I. Dunkl [a], U. Kempe [b], D. Stockli [c], M. Wiedenbeck [d], H. von Eynatten [a]

[a] University of Göttingen, Geoscience Center, Sedimentology and Environmental Geology, Goldschmidtstr. 3, 37077 Göttingen, Germany
[b] TU Bergakademie Freiberg, Institut für Mineralogie, Freiberg, Germany
[c] The University of Texas at Austin, Department of Geological Sciences, Austin, USA
[d] Helmholtz-Zentrum Potsdam Deutsches GeoForschungsZentrum, Potsdam, Germany

Received 11 September 2015; accepted in revised form 17 May 2016; Available online 24 May 2016

Abstract

Precise analysis of the diffusion characteristics of helium in fluorite is crucial for establishing the new fluorite (U–Th–Sm)/He thermochronometer (FHe), which potentially provides a powerful tool for dating ore deposits unsuitable for the application of conventional geochronometers. Incremental helium outgassing experiments performed on fluorites derived from a spectrum of geological environments suggest a thermally activated volume diffusion mechanism. The diffusion behaviour is highly variable and the parameters range between $\log D_0/a^2 = 0.30 \pm 0.27\text{–}7.27 \pm 0.46\ \mathrm{s}^{-1}$ and $E_a = 96 \pm 3.5\text{–}182 \pm 3.8$ kJ/mol. Despite the fact that the CaF_2 content of natural fluorites in most cases exceeds 99 weight percent, the closure temperature (T_c) of the fluorite (U–Th–Sm)/He thermochronometer as calculated from these diffusion parameters varies between 46 ± 14 °C and 169 ± 9 °C, considering a 125 μm fragment size. Here we establish that minor substitutions of calcium by rare earth elements and yttrium (REE + Y) and related charge compensation by sodium, fluorine, oxygen and/or vacancies in the fluorite crystal lattice have a significant impact on the diffusivity of helium in the mineral. With increasing REE + Y concentrations F vacancies are reduced and key diffusion pathways are narrowed. Consequently, a higher closure temperature is to be expected. An empirical case study confirms this variability: two fluorite samples from the same deposit (Horni Krupka, Czech Republic) with *ca.* 170 °C and *ca.* 43 °C T_c yield highly different (U–Th–Sm)/He ages of 290 ± 10 Ma and 79 ± 10 Ma, respectively. Accordingly, the fluorite sample with the high T_c could have quantitatively retained helium since the formation of the fluorite-bearing ores in the Permian, despite subsequent Mesozoic burial and associated regional hydrothermal heating. In contrast, the fluorite with the low T_c yields a Late Cretaceous age close to the apatite fission track (AFT) and apatite (U–Th)/He ages (AHe) from the same locality. Remarkably, thermal modelling of FHe yields comparable results to the well-established modelling based on AFT and AHe.

Keywords: Fluorite; Helium; Diffusion; Thermochronology

1. INTRODUCTION

(U–Th–Sm)/He thermochronology of accessory minerals like apatite and zircon can provide excellent constraints on low-temperature thermal histories. However, the use of this method is limited to rocks that contain these minerals. Especially in some ore deposits (e.g. greisens) apatite is often rare or lacking due to the typically low pH of the ore-bearing fluids. In contrast, fluorite is a common constituent in high- to low-temperature hydrothermal veins, in granites, pegmatites, carbonatites and alkaline intrusives, in stratabound deposits and in the cement of some clastic sediment. In particular, hydrothermal veins occur in a wide variety of geological settings, but such veins are often not

---

* Corresponding author at: University of Münster, Geology and Palaentology, Corrensstr. 24, 48149 Münster, Germany. Tel.: +49 1795022260.
E-mail address: rwolff@uni-muenster.de (R. Wolff).

http://dx.doi.org/10.1016/j.gca.2016.05.029
0016-7037/

well suited for apatite and zircon-based geochronology. The need to date the formation age of such ore deposits led to the development of isotopic techniques for fluorite geochronology using Sm/Nd (Chesley et al., 1991, 1994; Gigoux et al., 2015), and U–Th–Pb (Hofstra et al., 2000). Fluorite (U–Th–Sm)/He (FHe) thermochronology was introduced by Evans et al. (2005) and applied by Pi et al. (2005) and Siebel et al. (2009). A comprehensive dataset of FHe ages measured on samples from several ore deposits of the Erzgebirge (Germany/Czech Republic) along with FHe-based thermal modelling yielded constraints on the thermal history compatible with results from well-established thermochronometers such as apatite fission track and apatite (U–Th)/He (Wolff et al., 2015a,b).

The parameters controlling helium diffusion in fluorite, and thus the closure temperatures (T_c), are still under debate. Evans et al. (2005) published helium diffusion data on 200–350 μm diameter fragments of colourless fluorite. These measurements were accomplished by stepwise degassing between 215 °C and 335 °C. These authors suggested that volume diffusion is the dominant mechanism by which helium is released from fluorite. The observed deviation in the Arrhenius plot from linearity at higher temperatures was attributed to grain size effects, shape variability and/or defect/radiation damage density. The linear segment of their data yields an $E_a = 127.6$ kJ/mol and $\log D_0/a^2 = 4.9 \pm 0.6\ s^{-1}$ (at linearity of $R^2 = 0.9984$). These results correspond to a T_c of 60 °C ± 5 °C. In contrast, Peter W. Reiners' diffusion experiments (published in Pi et al., 2005) indicated a fluorite T_c of 200 °C. According to the empirical case study of Wolff et al. (2015a) the fluorite helium T_c is in the range of the thermal sensitivities of ZHe and AHe thermochronometers.

All of the above listed diffusion experiments are based on only very few data sets and the chemical composition of the studied specimens or other crystallographic characteristics were not reported. Yet, fluorite is famous for its broad variety in colour which results mainly from radioactive irradiation and the degree of substitution of calcium and fluorine in the crystal lattice, leading Evans et al. (2005) to suggest that variations in mineral colours may correlate with the diffusion characteristics of fluorite. However, the relation between colour and real structure (i.e. substitution of formula elements, vacancies, etc.) remains ambiguous (e.g. Dill and Weber, 2010). In order to shed light on this situation, we performed a detailed study on helium diffusion in fluorite using highly diverse samples derived from a variety of geological settings with variable genesis, precipitation temperatures, colours, habits and REE distribution patterns. The associated differences in T_c were constrained in a case study where distinct FHe ages from natural fluorites from one deposit with differing T_c could be compared.

2. SAMPLE SELECTION

Using the (U–Th–Sm)/He method, we have dated over 660 fluorite crystal aliquots from 112 samples originating from 58 localities (Wolff et al., 2015a). Sample selection for diffusion experiments was based on this data set because proper test material needs to be homogeneous, free of inclusions, and should contain sufficient helium to allow multi-step degassing experiments. Decrepitation experiments were performed on 7 samples, whereas diffusion experiments were performed on 34 aliquots from 14 samples (Table 1). Beyond 'near stoichiometric' fluorites, we performed diffusion experiments on samples with unusual compositions including Y-rich fluorite (sample K2), brownish, thorium-rich fluorite (SD1001), "black" (dark pink), stink-fluorite (RW-5-11), and sodium-and REE-rich green fluorite (HK13). Most of the samples were characterised in detail in earlier studies, e.g. fluorites from tin and polymetallic deposits in the Erzgebirge (Zinnwald, Horni Krupka, Sadisdorf, and Lauta; see Kempe et al. (2002), Wolff et al. (2015a)), from Usakos, Namibia (Bühn et al., 2002, 2003), from the giant Be-deposit Ermakovka, Transbaikalia (Kempe and Götze, 2002), and from the W-deposit of Kyzyltau, Mongolian Altai (Kempe and Belyatsky, 2000). Samples from inaccessible mining sites in the Erzgebirge could be obtained from the mineral collection of the Technische Universität Berkakademie Freiberg.

3. METHODS

3.1. Mineral chemistry

The concentrations of 27 cations were determined on same aliquots previously used for diffusion experiments and age dating. The dissolved fluorite aliquots were analysed using externally calibrated solution ICP-MS analyses (see data in Electronic Appendix EA1). The chemical composition was determined on inclusion free crystal fragments of *ca.* 13–338 μg (average 72 μg). The sensitivity and resolution of this technique is between classical wet chemical analyses performed on powdered samples consisting of several hundred mg and the laser ablation technique that consumes less volume, but has considerably higher uncertainty. Additionally, the laser ablation method is typically not viable for fluorite because of the low adsorption of UV light in the mineral, frequent fragmentation and small explosions that occur during ablation.

We also investigated whether variations in trace levels of anions might influence He diffusion rates in fluorite. The CAMECA 1280-HR instrument at the Helmholtz-Zentrum Potsdam was used to establish variations in the C, O, P, S and Cl contents of six samples with variable REE, Y, and Na composition. Due to the lack of a suitable fluorite reference material, it was only possible to determine the relative abundances of these anionic species between the samples and the inter- and intra-crystalline variability of their concentrations within a single sample. By normalising to the observed $^{19}F^-$ count rate, our method was able to establish the relative concentrations of these trace elements over a range exceeding 10^5. The spot size diameter for a single analysis was roughly 10 μm with a total sampling mass in the low nano-gram range (for analytical parameters see EA2).

3.2. Cathodoluminescence spectra

A JEOL JSM 7001F scanning electron microscope (SEM) with a thermal field emission electron gun equipped with a GATAN MiniCL detector was used for CL imaging. The SEM was operated at 20 kV and 0.6 nA. CL spectra were obtained by means of a system consisting of a GATAN MonoCL 4 mirror, an optical fibre guide and a Princeton Instruments Acton SP 2300 monochromator equipped with a PIXIS 256 CCD. The SEM was operated at 20 kV and 1 nA with a defocused beam when taking spectra.

3.3. Helium diffusion experiments

The outer surface of euhedral crystals or crystal fragments was stained, and the samples were carefully crushed. Only intact, inclusion-free shards derived from the interior of the crystals were selected. The maximum stopping distance of alpha particles is estimated as 14.2 μm by NUDAT 2.6 (7/14/2014) data base and ranges calculated by the software programs ASTAR and SRIM (Ziegler et al., 2010; see EA3). Both size and shape parameters of the crystal fragments were determined by multiple microphotographs. The average fragment size used for diffusion experiments was between 100 and 400 μm and the radius value used for calculation of diffusion parameters refers to the maximum insphere dimension that can be constructed based on such photographs.

The step heating experiments were performed in two laboratories (University of Göttingen/Germany and Jackson School of Geoscience, University of Texas in Austin/USA) using slightly different instruments and degassing schedules. In both laboratories the helium diffusion experiments were based on the stepwise degassing apparatus of Farley et al. (1999). The single- and multi-fragment aliquots were placed in *ca.* 1 × 1 mm-sized platinum capsules prior to stepwise degassing under high vacuum.

In the Göttingen laboratory, the heating was performed by PID-controlled low voltage gold covered halogen lamps. The steps were chosen for the samples individually considering the former dating experiments in order to provide convenient amounts of He through the entire degassing procedure. The samples were held at the respective heating temperature reached between the single steps to avoid thermal stress of the crystals and reduce the thermal hysteresis. The temperature was raised from 280 to 520 °C in 20 °C steps for most samples (EA4). Beforehand, seven samples were studied in decrepitation experiments (for experimental details see EA5 and Burlinson, 1991) in order to assign the temperature range where diffusion experiments can be performed without significant fragmentation and subsequent change of the diffusion domain size of the fluorite crystals. As intense decrepitation initiates at *ca.* 300 °C (EA5), the starting temperature for diffusion experiments was chosen to be as low as 150–280 °C. Accordingly, the first diffusion steps should be unaffected by decrepitation that might change the size of the diffusion domain. However, at higher temperatures it possibly overlaps with diffusion experiments. Interestingly, at temperatures where the decrepitation events reach a maximum, in some cases (e.g. sample K2) the diffusion experiments showed minor deviations from linear behaviour. Even though there are uncertainties, e.g. the shorter temperature holding time and not using high vacuum, the experiments emphasise the importance of careful selection of inclusion-free fluorite fragments and of checking the integrity of the crystals after the diffusion experiments to minimise the possible influence of helium liberated from fluid inclusions.

Temperature cycling experiments had been used to investigate whether complex heating schedules yield comparable results to the method using monotonic increasing temperature steps. Therefore, a decrease and increase in 40 °C steps for two hours after the first sequence was chosen (for detailed heating schedule see EA4). The extracted gas was purified and analysed as described in Section 3.4, below (see also Wolff et al., 2015a). Following the stepwise degassing, the Pt capsules were totally degassed by reheating with an infrared diode laser. Subsequent dissolution, spiking and actinide measurements were identical to the procedure applied for the (U–Th–Sm)/He dated crystals (Wolff et al., 2015a; see below).

In the Austin laboratory, total cooling was applied between the heating steps while the extracted gas was purified in a cryo-trap (see also Stockli and Farley, 2004). At least two heating cycles between 150 °C and 550 °C in 10 °C steps were performed at all samples. The purified gas was analysed by a Pfeiffer mass spectrometer. The actinide and Sm contents of the dissolved (HCl and HNO_3) and spiked solution were measured with an Element 2 mass spectrometer.

Diffusion parameters E_a and D_0/a^2 were calculated using the Eqs. (5a–c) of Fechtig and Kalbitzer (1966). If this diffusion process is exponentially activated by temperature the overall temperature dependence can be described by a linear Arrhenius relationship:

$$D = D_0 \exp\left(-\frac{E_a}{RT}\right) \qquad (1)$$

Hereby, T is the temperature, E_a the activation energy in the sense of Arrhenius, and D_0 the diffusivity at infinite high temperatures (frequency factor) (Eq. (1)). The T_c has been calculated after Dodson (1973) with the assumption of a spherical geometry and 10 °C/Ma cooling rate. For regression and uncertainties Monte Carlo inversion has been applied using the Matlab code of Goldsmith and Stockli (version 2, available on request at DS, for further details see EA6).

3.4. Fluorite (U–Th–Sm)/He thermochronology

The fluorite (U–Th–Sm)/He method is based on the He accumulation from the radioactive decay of ^{147}Sm as well as that which accumulates from the ^{238}U, ^{235}U and ^{232}Th decay chains. The alpha-ejection correction (Farley et al., 1996) was not applied, because fragments from the outer surface of the crystals had been excluded from the analyses. We dated only single-fragment aliquots; the crystal fragments were wrapped in *ca.* 1 × 1 mm-sized platinum capsules and totally degassed in high vacuum by heating with an infrared diode laser. The extracted gas was spiked with ^{3}He and purified using a SAES Ti-Zr getter at 450 °C. The chemically inert noble gases and a minor amount of other trace gases were then expanded into a Hiden triple-filter quadrupole mass spectrometer equipped with an ion counting detector. Crystals were checked for degassing of helium by sequential reheating and helium measurement. We assume that the loss of the actinide elements during the thermal treatment was negligible. Due to their high atomic masses the diffusion of U and Th is even slower than it was determined for REEs by Cherniak et al. (2001). Following degassing, samples were retrieved from the gas extraction line, the crystals were removed from Pt capsules and spiked with calibrated ^{230}Th and ^{233}U solutions. The fluorites were then dissolved in open Savillex Teflon® vials using ultrapure 30% HCl at 75 °C for 24 h (until totally dry). The dissolution process was monitored by a stereo microscope and the last step was repeated until total digestion was achieved. The digested samples were taken up in 4% HCl and the solutions were analysed using a Perkin Elmer Elan DRC II ICP-MS equipped with an APEX micro-flow nebulizer. The actinide concentrations were determined by isotope dilution and the Sm and other elements by external calibration. The typical uncertainties of the actinide measurements range between 1.4% and 2.3% and for the externally calibrated elements between 4% and 5%. The level of detection (LoD) was between 1 and 2 pg, slightly variable in the different ICP-MS sessions.

4. RESULTS

A synopsis of the results of the experiments is given in Table 1. The details of the diffusion experiments and calculations, the fluorite (U–Th–Sm)/He data, and the cation and anion concentrations are presented in the Electronic Appendices 1–7.

4.1. Chemical composition of the fluorite samples

4.1.1. Cations

The most abundant cations in fluorite have been monitored in our study (details in EA1). The sum of rare earth elements and yttrium (REE + Y) contents of the 34 fluorite aliquots commonly range between 66 ± 1 and 8,782 ± 73 μg/g (RW-2-8b, HK13). However, one extreme Y-rich fluorite sample with an average of 112,773 ± 2297 μg/g REE + Y has also been analysed (K2). This sample has the least internal variation in chemical composition. Sodium contents range from 33 ± 6 to 5563 ± 0.5 μg/g for samples RW-4-7 and K2, respectively.

4.1.2. Anions

The relative concentrations of the anions C, O, F, P, S and Cl were analysed in seven samples (EA2) by SIMS (results are listed in EA7). By normalising the observed count rates to that of $^{19}F^-$ (from 3.0*10^8 to 5.7*10^8 counts per second), the variations of the other anions could be established. The $^{16}O^-/^{19}F^-$ ratio is at least two orders of magnitude higher than the other anion/F-ratios. The $^{35}Cl^-/^{19}F^-$ vs. $^{16}O^-/^{19}F^-$ ratios from the seven fluorite samples show distinct clusters (Fig. 1).

4.2. The alpha-emitting elements in fluorites

The 34 analysed fluorite aliquots contain between 0.007 and 57 μg/g U, 0.05 and 5563 μg/g Th, and 0.3 and 1101 μg/g Sm. The averages are 8 μg/g U, 745 μg/g Th and 221 μg/g Sm. It was suggested earlier that, because U cannot be easily incorporated in the fluorite structure, only Th^{4+} and Sm^{2+}/Sm^{3+} readily substitute for Ca^{2+} (Kempe et al., 1994). Accordingly, Th and Sm are the main contributors to the total radiogenic He production in most cases (Fig. 2). In this study, we use a parameter eU* instead of the commonly used effective U content (eU = U μg/g + 0.253 * Th μg/g). The new parameter also takes into account the contribution from Sm (eU* = U μg/g + 0.253 * Th μg/g + 0.005 * Sm μg/g). In the samples used for diffusion experiments, the eU* ranged between 1 and 1367 μg/g. Remarkably, samples K2, KN6 and RW-4-7 show very homogeneous internal distributions of the radioactive elements. In samples RW-5-11, RW-2-8b, c and YM6, U contributes significantly to the total radiogenic He. Sm is the main source of the radiogenic He only in samples KT26 and YM6.

4.2.1. Cathodoluminescence

Two fluorite samples RW-5-11 and RW-4-7 were additionally analysed by cathodoluminescence (CL) imaging and spectroscopy (Fig. 3) to establish their internal textures and characteristics of the related defect structures (Kempe and Götze, 2002). Most other samples used in this study have been previously characterised by the same methods (Kempe et al., 2002; Wolff et al., 2015a) including RW-2-22c, RW-2-8c, RW-5-11, HK13, ED1b, K2, KN6, KT26, SD1001, SD1004b, YM6, and ZW315/2g. Here we highlight results from key samples that are relevant to the discussion of diffusion characteristics. Kempe et al. (2002) described patchy secondary alteration replacing primary growth zoning for green fluorite in sample ZW315/2g. This fluorite sometimes included brownish fluorite and is rimed by pink Fluorite ZW315/2g. Sample SD1001 represents rare Th-rich, brownish fluorite. CL imaging revealed the occurrence of a microbreccia, interpreted to be related to the formation of a breccia pipe within the Sadisdorf tin deposit. The sample RW-5-11 shows complex textures with broken crystals in the interior, growth zoning in the outer regions and fibrous textures in pink zones (Fig. 3). RW-4-7 is more homogeneous and shows frequent pinkish zoning.

4.3. Diffusion behaviour

The results of the 34 diffusion experiments are presented as Arrhenius plots in Figs. 4–7 (for details see EA6) and as calculated diffusion parameters in Table 1. For diffusion experiments mainly green fluorites were chosen because such fluorites are usually richer in Th and Sm than samples having other colours, and consequently sufficient helium for the multi-step degassing. However, pink, colourless, brown and dark pinkish-black fluorite samples were also studied

Table 1
Synopsis of locality, colour, number of analysed crystals, diffusivities, activation energies, closure temperatures, REE + Y content, effective U content (eU*, see text for explanation), and sodium content of the studied fluorite samples.

Sample	Country	Locality	Colour	Lat. [° North]	Long. [° East]	Number of diff. Exp. Goe/Austin	Sample average													
							log(D_0/a^2) [s^{-1}]	± [s^{-1}]	E_a [kJ/mol]	± [kJ/mol]	T_c [°C]	± [°C]	REEY [µg/g]	s.e. [µg/g]	eU* [µg/g]	s.e. [µg/g]	Na [µg/g]	s.e. [µg/g]		
ED1b	Erzgebirge	Ehrenfriedersdorf	Green	50.6439	12.9813	*1/0*	0.75	0.3	101	3.4	57	8.5	399	–	*0.1*	–	61	0.5		
HK13	Erzgebirge	Horni Krupka	Green	50.7165	13.8550	5/2	5.89	0.5	168	5.8	143	7.6	7358	817	*10.7*	3.6	1002	0.3		
K2	Keijv		Colourless	–	–	4/0	6.93	0.1	168	1.4	123	1.5	112773	1077	*1077.0*	268	5563	0.5		
KN6	Kazakhstan	Pegmatite of Kent	Green	–	–	3/2	4.17	0.5	150	7.4	129	10.1	*1950*	*351*	*2.5*	0.2	179	0.6		
KT26	Mongolia	Kyzyltau	Pale green	–	–	2/0	1.78	1.1	111	13.2	66	19.1	8521	35	*1.3*	0.3	380	4.5		
RW-2-8b	Erzgebirge	Lauta	Pink	50.6634	13.1544	1/0	*1.78*	*0.1*	*104*	*1.9*	*47*	*5.6*	*66*	–	*0.1*	–	*139*	6.6	+	
RW-2-8c	Erzgebirge	Lauta	Pink	50.6634	13.1544	1/0	*0.96*	*0.2*	*112*	*2.9*	*88*	*7.5*	*507*	–	*2.5*	–	*90*	7.7	+	
RW-4-7	Namibia	Sandamab, Usakos	Green	–	–	7/0	3.21	0.2	128	1.3	89	5.1	671	94	*9.6*	3.9	33	5.6		
RW-5-10	Erzgebirge	Horni Krupka	Colourless	50.7165	13.8550	–	–	–	–	–	–	–	224	–	*1.1*	0.4	–	–	+	
RW-5-11	Erzgebirge	Zinnwald	Dark pink	50.7165	13.8550	2/1	1.52	0.8	111	11.1	71	16.6	67	1	*5.9*	0.2	171	1.6	+	
RW-5-7	Erzgebirge	Horni Krupka	Colourless	50.7165	13.8550	–	–	–	–	–	–	–	125	–	*0.0*	–	–	–	+	
RW-5-8	Erzgebirge	Horni Krupka	Colourless	50.7165	13.8550	*1/0*	3.09	0.5	110	5.1	43	14.1	147	–	*0.4*	–	78	5.3	+	
RW-5-9	Erzgebirge	Horni Krupka	Honey	50.7165	13.8550	–	–	–	–	–	–	–	1353	–	*0.1*	0.0	–	–	+	
SD1001	Erzgebirge	Sadisdorf	Brown	50.8251	13.6463	1/0	*2.40*	*0.3*	*117*	*3.8*	*73*	11.0	224	–	*17.4*	–	*565*	–	+	++
SD1004b	Erzgebirge	Sadisdorf	Brown	50.8251	13.6463	*1/0*	*3.85*	*0.2*	*128*	*2.2*	*77*	6.0	1086	–	*36.6*	–	108	9.8		
YM6	Transbaikalia	Yermakovka	Green	–	–	*1/0*	*3.12*	*0.2*	*113*	*2.1*	*50*	6.0	5446	–	*1.0*	–	*1022*	1.1		
ZW315/2g	Erzgebirge	Zinnwald	Green	50.7294	13.7675	*1/0*	*3.72*	*0.2*	*144*	*3.0*	*124*	8.0	*1233*	–	*0.8*	–	*220*	–	+	++

Goe/Austin: diffusion experiment performed in University of Göttingen/University of Texas, Austin; Numbers in italics represent fluorite samples, where only one crystal yielded usable information; (+) Age and REE+Y published in Wolff et al. (2015a); (++) Na content from AAS.

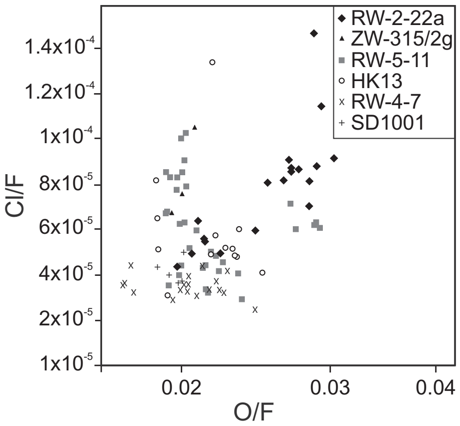

Fig. 1. Ratio of O/F versus Cl/F (ion counting ratios not corrected for variation in ion yields) indicate cluster of internally more homogeneous fluorite samples (e.g. SD-1001, RW-4-7) and heterogeneous samples, measured by SIMS.

by diffusion experiments (Table 1). The analysed aliquots contained from 0.8 to 5102 ncc [nano-cubic centimetres, equivalent to 10^3 μm^3] helium; in the diffusion experiments between 11.8 and 99.8 vol% of the total helium was released, in most cases more than 75% (EA4). In order to calculate diffusion parameters, a linear segment on the Arrhenius plot needs to be identified (e.g. McDougall and Harrison, 1988). The first isothermal steps were, in most cases, disregarded as they released unreasonably high amounts of helium. Such inconsistent results during the first fractional release steps (typically less than 2.5% of the total released He) is probably related to surface roughness and irregularities as described by Farley (2000). Subsequent heating steps of the first monotonic heating sequence (bold in EA4) revealed a strong linear relationship between $\ln D_0/a^2$ and inverse temperature with an R^2 between 0.947 and 0.999 on 34 to 2 degrees of freedom with an average of 8 (Figs. 4–7). The higher temperature steps were only rejected when they clearly deviated from the linear segment, resulting in a decreasing in the coefficient of determination (R^2) by 0.004 (regular in EA4). The calculated helium diffusion parameters of fluorites from the linear segments yielded a range of $\log D_0/a^2 = 0.30 \pm 0.27\text{–}7.27 \pm 0.46\ s^{-1}$. The corresponding activation energy ranges between $E_a = 96 \pm 3.5$ and 182 ± 3.8 kJ/mol (EA6). This corresponds to a range in T_c from 43 ± 14 °C to 170 ± 9 °C (assuming a 10 °C/Ma cooling rate and sphere geometry). The second and, if performed, the third heating cycles yielded linear segments that commonly overlapped in the Arrhenius plot with the first.

Samples HK13 and K2 yielded the highest average $\log D_0/a^2$ with 6.6 ± 0.35 and $7.1 \pm 0.37\ s^{-1}$, respectively. The lowest $\log D_0/a^2$ values were 0.30 ± 0.27 and $0.97 \pm 0.22\ s^{-1}$ for samples RW-5-11 and RW-2-8c, respectively. Sample HK13 also has the highest average activation energy of 169 ± 13 kJ/mol, whereas the lowest recorded average value was 104 ± 1.90 kJ/mol for sample RW-2-8b. There is no indication for a simple correlation between diffusion characteristics and sample colouration despite a tendency to low activation energies in pink samples. The coluoration was held widely constant for a single sample by carful separation in cases when there is visible variation in the original specimen.

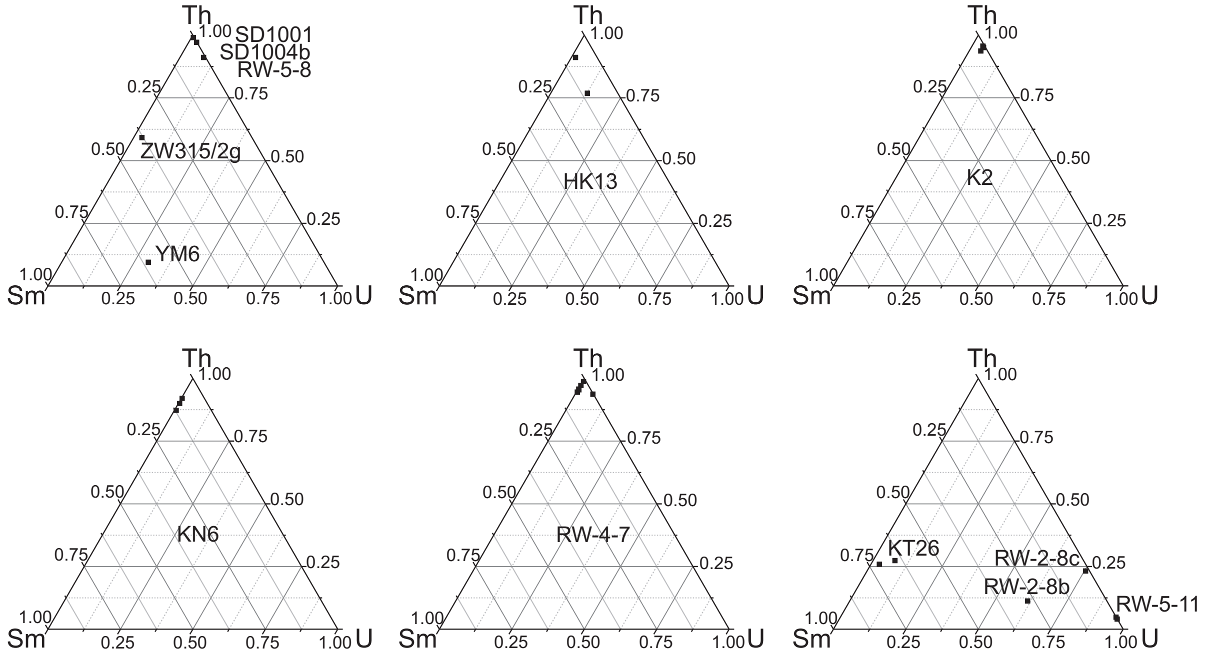

Fig. 2. The contributions of the three alpha-emitting elements to the total radiogenic helium budget of the analysed fluorites reveal those samples with dominant Th contribution. The homogeneous actinide content of the samples can be well identified.

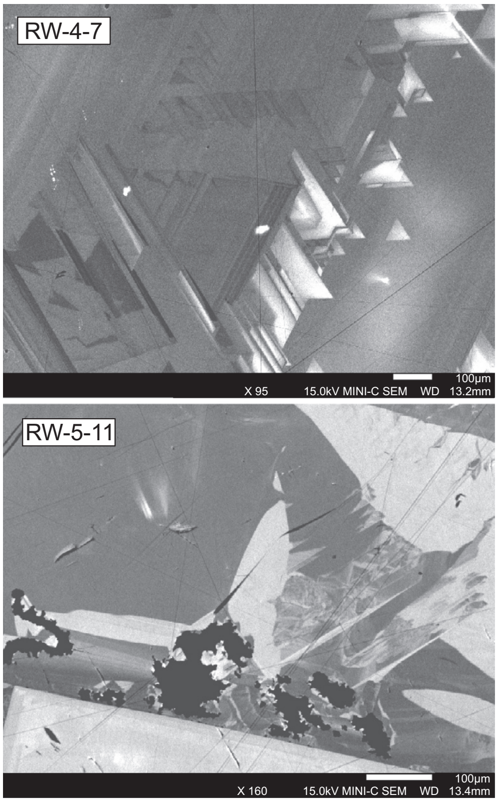

Fig. 3. SEM-CL images of fluorite: (upper) CL image of fluorite sample RW-4-7 (Namibia) with homogeneous patterns and skeletal zonation (lower) CL image of fluorite sample RW-5-11 (Zinnwald, Erzgebirge) with complex textures with broken crystals and primary zoning.

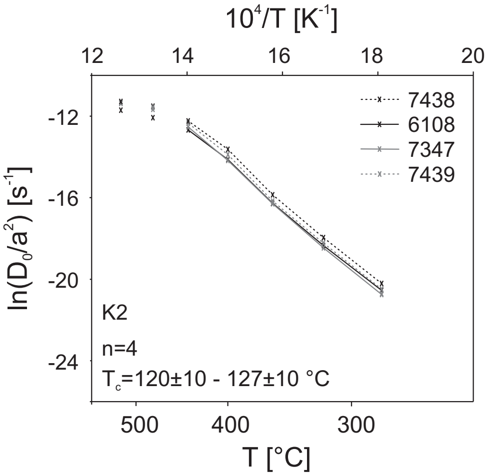

Fig. 4. Arrhenius plot of step-heating experiment of K2 fluorite sample (two high temperature steps are rejected due to their deviation from linear trend, for details see Section 5). The consistency of the diffusion results from differing aliquots of this sample demonstrates both the homogeneity of the material and the robustness of the experimental setup.

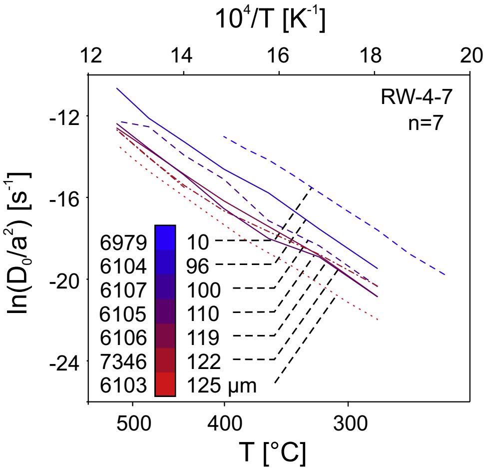

Fig. 5. Arrhenius plot of seven aliquots from sample RW-4-7 covering roughly one order of magnitude in grain size (colour scale from small to big, blue to red, respectively). With decreasing crystal size the diffusivity array shifts upwards. This is consistent with a relationship of the diffusion domain size and the grain size. (For interpretation of the references to colour in this figure legend, the reader is referred to the web version of this article.)

4.4. (U–Th–Sm)/He dating of a selected, complex locality

To verify the variations in T_c, an empirical case study was performed on fluorite samples from the Krupka tin deposit, Krušne Horí, Czech Republic. Thirteen aliquots of sample HK13 yielded a mean age of 290 Ma ± 10 Ma (EA7). The Th/U ratio of this sample varied between 23 and 34 and the average measured REE + Y content is 5277 ± 516 µg/g. The maximum eU* is 19 µg/g. From the same locality another sample was also studied that has a significantly lower REE + Y content of *ca.* 130 ± 28 µg/g. Nineteen fluorite aliquots of this fluorite yielded a mean (U–Th–Sm)/He age of 79 Ma ± 10 Ma (Wolff et al., 2015a).

5. DISCUSSION

First we will discuss both the Arrhenius plots of our data in general and the diffusion mechanism governing the loss of helium. Thereafter, we will address the reproducibility of the diffusion measurements and compare the results measured independently in two laboratories. After verifying the robustness of these results we will address the intrinsic factors affecting helium diffusion in fluorite, including diffusion domain size, radiation damage, and the chemical composition of the crystals.

5.1. Evaluation of laboratory diffusion data

5.1.1. Linearity in Arrhenius plots supports isotropic volume diffusion

In the simplest and isotropic case – which should be expected in a first approximation for fluorite due to its cubic crystal lattice symmetry – helium would move through a crystal only by volume diffusion governed by a

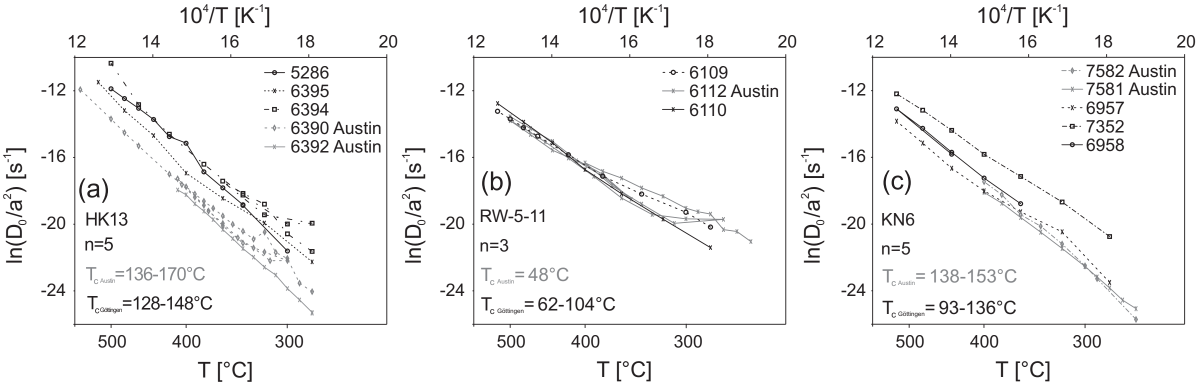

Fig. 6. Comparison of the experiments generated in the Austin (grey) and Göttingen (black) laboratories: Arrhenius plots of step-heating He diffusion experiments on three different fluorite specimens (a: HK13, b: RW-5-11, and c: KN6) and calculated T_c (grey: Austin, black: Göttingen). Although the grain sizes are comparable the diffusion arrays of Austin are lower for the sample HK13, whereas they overlap well for the other two samples.

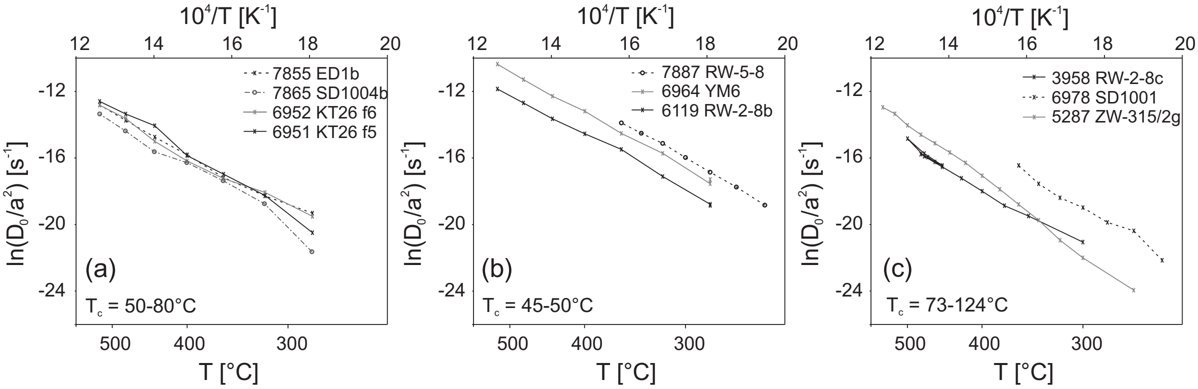

Fig. 7. (a) Samples ED1b, KT26, SD1004b with intermediate T_c. (b) Samples YM6, RW-2-8b, RW-5-8 with low T_c. (c) Samples SD1001, ZW315/2g, RW-2-8c with high T_c.

single, thermally activated process. Under such conditions, the temperature dependence of diffusivity can be characterised by a single activation energy and a single diffusivity value for an infinitely high temperature. If these conditions apply then bulk diffusion experiments over a given temperature range will yield a straight line on an Arrhenius plot. However, in more complicated cases such as anisotropy, multiple diffusion domains or fast diffusion pathways, the Arrhenius relation will not result in a straight line but instead in more complex patterns (e.g. changes in slope or curves; Reiners et al., 2002). The most important feature of our data is the obvious linear Arrhenius behaviour of all fluorites in the analysed temperature range from 150 to 550 °C (Figs. 4–7). Only one sample, K2, shows a very minor change in slope towards higher temperatures (Fig. 4). Such a change in slope at higher temperatures has been observed by Evans et al. (2005) in the case of fluorite, too, and might be indicative of insufficient mineral integrity, e.g. grain size effect, shape variability, and annealing effects of irradiation damage. We conclude that annealing might be the case here because K2 has received the highest radioactive dose (*ca.* $8.6*10^{18}$ alpha decay event/gram; see Section 5 below). In the interpretation of the diffusion data from sample K2 the two corresponding values showing this change in slope have been disregarded (Fig. 4). As the behaviour of all other samples supports the single activation energy assumption, yielding excellent correlations ($R^2 > 0.947$), there is very strong evidence that only a single, isotropic diffusion mechanism may be regarded responsible for the diffusional loss of He in fluorite, namely thermally activated volume diffusion. Besides, because of the cubic crystal symmetry it is unlikely assuming anisotropic diffusion.

5.1.2. Complex heating schedules confirm the robustness of results

For 17 samples (marked in the last column in EA6 and details in EA4), after the initial stepwise degassing using a monotonic heating sequence, we performed one or more additional heating cycles by repeatedly reducing and increasing temperatures (Farley, 2000). The prograde heating steps of these extended temperature cycling experiments yielded indistinguishable diffusion parameters from the monotonic heating experiments (e.g. Figs. 5–7, EA4). The retrograde steps resulted in slightly more scatter, but we did not observe systematic deviation from the prograde steps. This observation form the prograde steps confirms that He diffusivity is independent of the cumulative fraction of gas released and the chosen heating schedules. Furthermore, it indicates that there was no phase transformation or fragmentation of the crystals during the initial degassing experiments. These findings, together with the observed strongly linear behaviour ($R^2 > 0.947$), excludes a multi-diffusion domain (MDD) model (Lovera et al., 1989), which explains the deviation from a linear Arrhenius trend by a non-homogeneous population of diffusion domain sizes. The remaining 17 samples of our set were only step-heated to a temperature of 550 °C once, because by then the fluorite samples lost most of their He. Hence, a subsequent cooling and temperature cycling was not possible for these samples, which may have introduced a certain bias in our dataset. However, this bias in the dataset cannot be significant, as samples degassed by single and multiple heating cycles allow to draw the same conclusion. Applying more heating cycles by using proton induced ^{3}He would offer the means of improving such diffusion experiments in the future (e.g. Shuster and Farley, 2003; Tripathy-Lang et al., 2015).

5.1.3. Repeated measurements and the reliability of diffusion experiments

In order to obtain information about analytical reproducibility, from five samples between 2 and 7 aliquots were measured in the Göttingen laboratory. Four aliquots of sample K2 yielded the least variation: $E_a = 164 \pm 4.3$–170 ± 4.4 kJ/mol and $\log D_0/a^2$ 6.6 ± 0.35–7.1 ± 0.37 s^{-1} corresponding to a T_c of 120 ± 10–127 ± 10 °C (Table 2; Fig. 4). We interpret these consistent results as the consequence of the chemical and defect homogeneity of the K2 sample as revealed by our cation analyses (EA1) and CL studies. The broader spread in parameters observed between aliquots from the other samples is governed mostly by chemical-crystallographical heterogeneities. Thus, we can estimate the reproducibility of the laboratory diffusion experiments from the spread of the results yielded by the most homogeneous sample. Following this approach the method reproducibility would be approximately ±6 kJ/mol for E_a, ±0.5 s^{-1} for $\log D_0/a^2$, and ±7 °C for T_c.

5.1.4. Inter-laboratory comparison: accuracy of diffusion experiments

Samples HK13, KN6 and RW-5-11 were analysed in two laboratories in order to constrain the role of laboratory bias (Fig. 6). The diffusion arrays overlap in the Arrhenius plot for sample RW-5-11 and KN6 (Fig. 6b, c), however, even though the aliquot sizes are comparable (Austin: 117 μm, 138 μm and Göttingen: 119.5 μm, 126 μm, and 153 μm), the array of the Austin analysis plot systematically below the Göttingen results for sample HK13 (Fig. 6a). Comparing the calculated diffusivities and activation energies, both laboratories show wide spreads (Table 3). In the case of HK13, the E_a parameters are in agreement but the diffusivities in the Göttingen laboratory are slightly higher. The E_a value determined in the Austin laboratory was lower for RW-5-11 and higher for KN6, relative to those determined in Göttingen. Such variability may be due to the differences in heating schedule protocols. In Göttingen, the sample was held at temperature during the He measurement whereas in Austin, the sample was allowed to cool down between steps. We assume that the latter heating schedule, implying higher temperature variations, generates more thermal expansion and sub-microscopic fractures in the crystal. The induced fast paths along with a decrease in diffusion domain size could have increased the overall diffusivity. These different heating strategies might additionally contribute to the observed difference in HK13. However, inter-aliquot heterogeneity, different extraction cell volumes or dissimilar temperature measurement methods cannot be ruled out as possible explanations. The resulting variation between the different laboratories seems to be minor compared to the influence of the heterogeneity of fluorite itself (see next section). We conclude that the observed differences in the results are not reliable evidence for inherent systematic biases between the two laboratory set-ups.

Table 2
The major results of the diffusion experiments and the REE + Y content of sample K2 (the Arrhenius plot is presented in Fig. 4).

Sample K2	$n = 4$
$\log D_0/a^2$ [s^{-1}]	6.6 ± 0.35–7.1 ± 0.37
E_a [kJ/mol]	164 ± 4.3–170 ± 4.4
T_c [°C]	120 ± 10–127 ± 10
REE + Y [μg/g]	109,193 ± 917–119,515 ± 1382

5.1.5. Variations of the diffusion parameters in the different fluorite samples

The total range between the analysed fluorite aliquots is $E_a = 86$ kJ/mol and $\log D_0/a^2$ 6.13 s^{-1} corresponding to a T_c range from 169 to 46 °C (considering a 125 μm fragment size of all studied fluorite, for details see Table 4). The two samples with the lowest T_c, YM6 and RW-2-8b, show low E_a values (113 ± 2.1–104 ± 1.9 kJ/mol, Fig. 7b). Sample KT26 with a slightly higher T_c has also a low E_a of 111 ± 13.2 kJ/mol (Fig. 7a). The samples with an intermediate T_c between 90 and 125 °C have considerably higher E_a (130–145 kJ/mol) and also high diffusivities ($\log D_0/a^2$ 3.27–4.03 s^{-1}, Fig. 7c). Samples HK13 and K2 possess the highest diffusivities ($\log D_0/a^2$ 5.59–5.87 s^{-1}), and these also yielded the highest T_c. Such variations in both activation energy and diffusivity between the samples is much larger than the reproducibility of the diffusion measurements conducted on K2 (Fig. 4) and the inter-laboratory differences discussed above.

We conclude that our results are robust and that differences in diffusion parameters between different fluorite varieties really exist, and that such differences greatly exceed the uncertainty of our analytical methods. Moreover, the data agree with the previously published range in T_c (Evans et al., 2005; Pi et al., 2005). Obviously, helium diffusion in fluorite is variable just as in the case for the well-studied phases apatite (e.g. Farley, 2000; Shuster et al., 2006a;

Table 3
The major results of the diffusion experiments of three fluorite samples analysed in two different laboratories (see Arrhenius plots presented in Fig. 6).

Sample	Göttingen	Austin
HK13	$n = 3$	$n = 2$
Log D_0/a^2 [s^{-1}]	5.5 ± 2.3–7.3 ± 0.46	4.1 ± 0.15–6.2 ± 0.32
E_a [kJ/mol]	162 ± 3.1–181 ± 6.2	151 ± 1.9–182 ± 3.8
T_c [°C]	128 ± 6–148 ± 14	136 ± 5–170 ± 9
RW-5-11	$n = 2$	$n = 1$
Log D_0/a^2 [s^{-1}]	1.1 ± 0.19–3.2 ± 0.26	0.30 ± 0.27
E_a [kJ/mol]	105 ± 2.7–133 ± 3.5	96 ± 3.5
T_c [°C]	62 ± 7–104 ± 10	48 ± 6
KN6	$n = 3$	$n = 2$
Log D_0/a^2 [s^{-1}]	3.09 ± 0.26–4.48 ± 0.31	3.95 ± 0.54–6.01 ± 0.63
E_a [kJ/mol]	130 ± 2.5–154 ± 4.2	151 ± 6.4–173 ± 7.3
T_c [°C]	93 ± 7–136 ± 11	138 ± 17–153 ± 18

Table 4
Summary of the results from the diffusion experiments on the various fluorite samples.

	$n = 34$
Log D_0/a^2 [s^{-1}]	0.30 ± 0.27–7.27 ± 0.46
E_a [kJ/mol]	96 ± 3.5–182 ± 3.8
T_c [°C]	43 ± 14–170 ± 9
REE + Y [µg/g]	66 ± 1.5–119,514 ± 1382.4

Shuster and Farley, 2009) and zircon (e.g. Reiners et al., 2002; Flowers et al., 2009; Gautheron et al., 2009).

5.2. Possible factors influencing He diffusion

5.2.1. *Influence of diffusion domain size*

If the diffusion domain (DD) is equal to the physical size of the crystal, then the diffusivity array in the Arrhenius plot shifts down with increasing crystal radius. If the effective DD is much smaller than the crystal, then diffusivity is independent of the dimensions of the crystal (e.g. Farley, 2000). This model can be tested by diffusion experiments performed on aliquots of different fragment sizes taken from the same crystal. If aliquots of different grain sizes plot on the same line in the Arrhenius plot, then the DD is smaller than the physical dimensions of the analysed crystal fragments whereas if they yield different y-axis intercepts then the DD is larger than the size of the biggest analysed aliquot. Diffusion parameters were determined on seven multi-fragment aliquots made from sample RW-4-7 with different radii (10–125 µm). This particular is ideal for such an experiment due to its homogeneity (see REE + Y and CL imaging, Fig. 3, upper panel). The results are presented in Fig. 5 and show that with increasing crystal radii, diffusivity decreases. The difference in diffusivity for the aliquots is *ca.* 4.5 ln units in total (Fig. 5). This agrees well with the expected difference, which is predicted by D_0/a^2 of $(125/10)^2 = 156$. Hence, the diffusion domain is definitely larger than 125 µm, and it would be reasonable to assume the whole crystal acts as a single domain. Therefore, the T_c given in this publication is valid for the analysed fragment sizes and has to be corrected if applied to bigger crystals. For example, the measured T_c on a 125 µm fragment increases by *ca.* 60 °C in the case of a 0.5 mm mono-crystal, composed of a single diffusion domain.

5.2.2. *The possible influence of radiation damage density*

A possible explanation for variability in diffusion parameters is the accumulation of radiation damage (e.g. Nasdala et al., 1995). In the case of the commonly used apatite and zircon helium thermochronometers, the role of damage density is well studied (e.g. Shuster et al., 2006a,b; Flowers et al., 2009; Gautheron et al., 2009; Shuster and Farley, 2009). Alpha particle recoil damage is the most important factor in these cases and can be quantified by the effective U concentration (Flowers et al., 2009). The accumulation of radiation-induced metamictization in zircon generates defects that are easily detected by the full width at half maximum of Raman peaks (Nasdala et al., 1995; Presser and Glotzbach, 2009). A finite amount of radiation induced damage produces isolated defects into which helium can be trapped, effectively retarding further diffusive migration. At some higher level of damage, amorphization will occur, effectively creating a network of fast diffusion pathways. Once such a network of interconnected pathways is established, diffusivity rapidly increases (Shuster and Farley, 2009). With increasing accumulated radiation damage zircon first increases its T_c, but, once above a given damage threshold, T_c decreases dramatically (Guenthner et al., 2013). In zircon this threshold where the radiation damage density strongly enhances He diffusivity is $\sim 2*10^{18}$ alpha decay events/g (Guenthner et al., 2013). Modelling shows a threshold of $1.6*10^{16}$ alpha decay events/g for interconnection of the damage zones in zircon (Nasdala et al., 2004; Ketcham et al., 2013). In our fluorite samples the average radiation dosage received is *ca.* $1*10^{15}$ alpha decay events/g. This value is several orders of magnitude below the threshold mentioned for enhanced He diffusivity in zircon and apatite. The only exception is the fluorite sample K2 with an extremely high dosage of $8.6*10^{18}$ alpha decay events/g. We used this sample to test the role of radiation on helium diffusion in fluorite. The change in slope at higher temperatures (*ca.* 440 °C) in the Arrhenius plot might indicate the onset of annealing of radiation damage in fluorite. But within the broad range of radiation damage analysed, we did not detect any systematic influence of radiation damage on the T_c. This strongly suggests that accumulated radiation damage is not the dominant control responsible for the variable T_c observed between the various fluorite samples.

5.2.3. The possible influence of the replacement of Ca by tri-valent REE cations

A plausible explanation for the observed variability in T_c is suggested by the correlation of the REE + Y content with the T_c (Fig. 8). REE + Y readily substitute for Ca^{2+} because they have almost identical ionic radii, but subsequently the different charges need to be compensated. In samples with non-extreme compositions (excluding the Y-rich fluorite K2 and the samples KT26, YM6), our data suggest a trend towards higher T_c with increasing REE + Y content. For the outlier sample K2, effects of clustering of REE + Y that occur with increasing REE + Y content might be responsible. Moore and Wright (1981) first described clusters of REE + Y in fluorite and Kazanskii et al. (2005) suggested that such clusters had a hexamer structure. Samples KT26 and YM6 are from Be and W ore deposits with highly unusual geochemical settings. They are the only fluorite samples that we analysed where Sm is the main contributor to the total radiogenic helium budget (Fig. 2). Nevertheless, a decreasing degree of Ca^{2+} substitution by REE + Y is apparently sufficient to decrease T_c and increase He diffusivity. Similar effects on diffusivities by lattice deformation have been postulated for other minerals e.g. by Bengston et al. (2012) and Farley (2007).

Our observations point to a chemical/crystallographic control on He diffusivity in fluorite. In particular, their potential to trigger charge compensation mechanisms should be considered. Möller et al. (1998) outlined four major anionic charge compensation mechanisms for the substitution of REE^{3+} and Y^{3+} for Ca^{2+}.

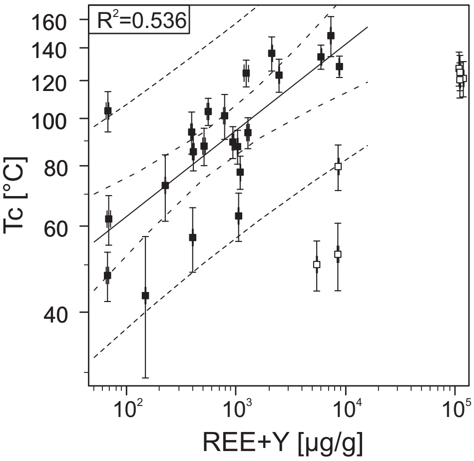

Fig. 8. Most prominent cations (REE + Y [µg/g]) substituting for Ca plotted against the closure temperature. With increasing REE + Y content a higher T_c can be expected. Samples represented by empty boxes are excluded from the calculation of the confidence interval – due to their extreme composition/genesis (KT26, YM6, and the Y-rich fluorite K2). Broken and dashed lines are the 95% confidence and prediction interval of the linear interpolation, respectively.

(i) $2Ca^{2+} = 2REE^{3+} + O^{2-}_{\text{replacing adjacent F-}}$
(ii) $3Ca^{2+} = 2REE^{3+} + \text{Ca-vacancy}$
(iii) $2Ca^{2+} = REE^{3+} + Na^{1+}_{\text{replacing neighbouring } Ca^{2+}}$
(iv) $Ca^{2+} = REE^{3+} + F^{1-}_{\text{F1, body-centred position}}$

Below we discuss the potential impact of these mechanisms on He diffusivity.

(i) For oxygen (as well as P, Cl, C and S) our SIMS data reveal no correlation between anion contents and the determined T_c. Noteworthy, the fluorite samples showed clusters, homogeneous internal distribution of the anion proportions based on O and Cl ratios (Fig. 1). Only sample RW-5-11 does not show distinct clusters, which is consistent with the heterogeneity observed by CL imaging (Fig. 3, lower panel).
(ii) Lattice vacancies, which might be expressed as ionic porosity (Dahl, 1997), and their distribution can either enhance diffusion by increasing mobility or act as energy wells trapping He and retard its mobility. Besides their "ambivalent" role, their quantification is not possible from our results.
(iii) The substitution of Ca by Na could result in a minor lattice deformation due to the slightly different ionic radii and, if this substitution is not compensated by REE + Y, it can create F vacancies. However, there is no obvious correlation between the Na/(REE + Y) ratio and the T_c (Table 1).
(iv) When tri-valent cation substitution is compensated by fluorine ions then the F1 body-centred positions of the lattice becomes occupied and the anion lattice became a mixture between CaF_2 and YF_3 (Nowacki, 1938). These additional F^- ions contribute to a retardation of diffusion along the pathways for helium and will have a direct influence on its diffusivity through the fluorite crystal lattice.

Although, the role of lattice vacancies is ambivalent, our data suggests two mechanisms explaining the significant variability of He diffusion in fluorite. (1) The expected position for the He released by radioactive decay in the fluorite lattice is the interstitial one in the empty F-coordinated hexahedrons of the structure. Diffusion may occur through the neighbouring interstitials (eight for every interstitial position, all equally likely) through two neighbouring fluorine ions (Nekrasov and Kupryashkin, 2001). Since the substitution of Ca by REE + Y is typically less than 1 weight percent, it is difficult to expect that this minor substitution compensated by (i), (iii), or (iv) may significantly affect the interstitial diffusion pathway of He. Situation changes when there is substitution of F^- by O^{2-} or Ca^{2+} by Na^+ not compensated by trivalent REE + Y. In these cases (detected in pink fluorite), we assume that resulting F vacancies may significantly enhance diffusion paths and lower the T_c as observed for several low-REE + Y samples in our study. Likewise, a quantitative excess of (neutral) fluorine F^0 occupying interstitial positions in the fluorite structure should reduce the diffusivity. Unfortunately, we have no hints for the second mechanism in or samples. (2) We assume that the Ca^{2+} vacancies formed by compensation mechanism (ii), in conjunction with the already existing empty F-coordinated hexahedrons, might act as energy wells trapping the helium atoms. In this case even <1 weight percent presence of vacancies is several orders of magnitude higher than the He concentration in the lattice. So, it can have easily a determinant negative effect on the mobility of He by trapping the gas atoms in the more abundant vacancies.

The available data suggest that the mechanism responsible for the variation in T_c is most probably related to the vacancy density in fluorite. Either, substitution not compensated by REE + Y increase the number of F vacancies enhancing He diffusion, or substitution generated Ca^{2+} vacancies trap He and excess F ions induce a narrowing of the available diffusion pathways. Hence, the REE + Y content can be used as proxy for the T_c.

6. TESTING VARIABLE CLOSURE TEMPERATURE IN AN EMPIRICAL CASE STUDY

The fluorite sample HK13 from Horny Krupka, Erzgebirge (Czech Republic), yielded an average FHe age and standard error of 290 Ma ± 10 Ma (Fig. 9). This is in close agreement with the mica Ar/Ar ages of between 314 ± 2 Ma and 312 ± 2 Ma for the Zinnwald and Horni Krupka Li–F granitoids (Seifert et al., 2011) and subsequent Permian rhyolitic volcanism (Romer et al., 2010). The analysed fluorite has greenish colour and high average REE + Y concentration of 5277 ± 516 µg/g. However, 19 aliquots from four fluorite samples from the same locality having lower amounts of REE + Y (*ca.* 130 ± 28 µg/g) gave FHe ages of 79 Ma ± 10 Ma (Fig. 9; Wolff et al., 2015a). Remarkably, both their REE pattern and their paragenesis point to the same genesis coupled to the granite intrusion in late Variscan times (Wolff et al., 2015a). The younger FHe ages are comparable to apatite fission track and (U–Th–Sm)/He ages of 98 and 103 Ma, respectively, from the same locality and thermal modelling of FHe yields comparable results (Wolff et al., 2015b). These ages reflect the timing of overall Cretaceous cooling for the entire Erzgebirge basement (Wolff et al., 2015b).

The calculated closure temperature for HK13 is the highest identified in our study (130–170 °C) while the younger sample (RW-5-8) yielded a considerably lower T_c of *ca.* 43 °C (Figs. 7 and 8). Due to their close proximity and the lack of evidence for any local perturbation of isotherms, it is concluded that these samples must have experienced the same thermal history. Moreover, FHe ages of the different samples yielded the age of the two most characteristic periods of thermal evolution of the region, namely post-Variscan cooling and Late Cretaceous exhumation and termination of hydrothermal activity (Voigt, 2009; Wolff et al., 2015b). After the Permian, the deposit was heated during burial above the low-REE fluorite's closure temperature (and even above the apatite He closure temperature), but the maximum temperature remained below the closure temperature of the high-REE fluorite.

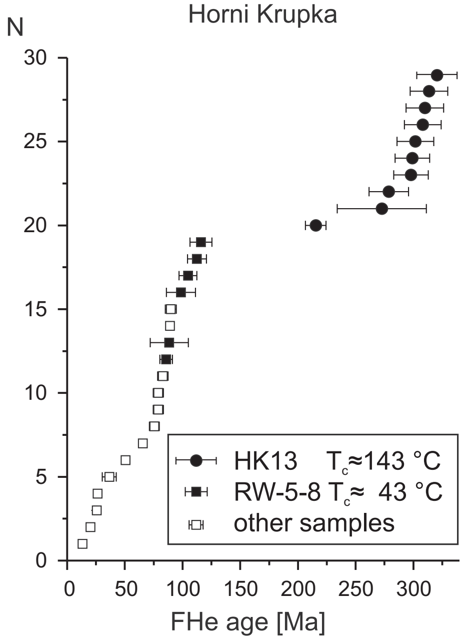

Fig. 9. Fluorite (U–Th–Sm)/He ages plotted in increasing order; the dated single-fragment aliquots derive from different samples of the Horni Krupka mining district. The bimodal age distribution corresponds well with the measured closure temperatures. The old ages actually resemble post-emplacement cooling, while the young age group reflects the age of the Cretaceous regional hydrothermal heating event.

The dependence of the He diffusivity on the chemical composition as predicted from the laboratory diffusion experiments is thus confirmed by the Horny Krupka case study.

7. CONCLUSIONS

Diffusion of helium in fluorite was measured by stepwise degassing in two laboratories on a large number of aliquots.

- The results are robust, although minor differences were detected between the laboratories using different analytical designs. This underlines the need for further cross-calibrations of different laboratory techniques.
- The linearity of the Arrhenius plots indicate a thermally activated volume diffusion. However, diffusivity of helium in different fluorite samples is highly variable and the determined closure temperatures range from 169 to 46 °C, considering a 125 µm fragment size of all studied fluorite.
- Fluorite formed in differing environments and with differing parageneses has variable degree of Ca^{-} > REE + Y substitution, but typically less than 1 weight percent. Further, the detected closure temperatures show a general correlation with the REE + Y contents. Therefore, the REE + Y content can be used as a proxy for the closure temperature.

- Our data allow us to draw the conclusion that most likely the decrease in closure temperature brought about by substitution not charge compensated by REE + Y results in increasing F vacancies probably enhancing the diffusion within the fluorite lattice. Additionally, the increasing proportion of the third fluorine ion is blocking the helium diffusion pathways due to its body centred position in the cubic YF_3-type crystal lattice. Further, we assume that substitution generated vacancies can have the effect of trapping He in the fluorite lattice.
- Laboratory-determined closure temperatures have been verified by an empirical case study: from one deposit two fluorites with different compositions and closure temperatures yielded different FHe ages. The 290 Ma and the 79 Ma data coincide with the Permian and Cretaceous cooling periods, which have been well-established for the region.

ACKNOWLEDGMENTS

This study was funded by the German Research Foundation (DFG grant DU373/6). We are greatful to Harald Dill (Hannover), the mineral collection at University of Freiberg and the Bergbaumuseum at Altenberg for the donation of mineral species. We are indebted to the Central Metal Workshop at Geoscience Center Göttingen for the maintenance of the GÖochron Laboratories and to Kingsley Burlinson for the decrepitation experiments (Burlinson Geochemical Services, Darwin, Australia). Frédéric Couffingal gave expert help during SIMS data collection. Special thanks to Adam Goldsmith for the diffusion experiments in Austin, Igor Villa (Milano, Bern), Noreen Evans (Curtin), and István Dódony (Budapest) for enlightening discussions. Thoughtful suggestions and comments by Stephen Cox and an unknown reviewer as well as careful editorial handling by David Shuster helped to improve the manuscript.

APPENDIX A. SUPPLEMENTARY DATA

Supplementary data associated with this article can be found, in the online version, at http://dx.doi.org/10.1016/j.gca.2016.05.029.

REFERENCES

Bühn B., Rankin A. H., Schneider H.-J. and Dulski P. (2002) The nature of orthomagmatic, carbonatitic fluids precipitating REE, Sr-rich fluorite: fluid-inclusion evidence from the Okorusu fluorite deposit, Namibia. *Chem. Geol.* **186**, 75–98.

Bühn B., Schneider J., Dulski P. and Rankin A. H. (2003) Fluid–rock interaction during progressive migration of carbonatitic fluids, derived from small-scale trace element and Sr, Pb isotope distribution in hydrothermal fluorite. *Geochim. Cosmochim. Acta* **67**, 4577–4595.

Burlinson K. (1991) Decrepitation in gold exploration. A case history from the Cotan prospect, N.T. *J. Geochem. Explor.* **42**, 143–156.

Bengston A., Ewing R. C. and Becker U. (2012) He diffusion and closure temperatures in apatite and zircon: a density functional theory investigation. *Geochim. Cosmochim. Acta* **86**, 228–238.

Cherniak D. J., Zhang X. Y., Wayne N. K. and Watson E. B. (2001) Sr, Y, and REE diffusion in fluorite. *Chem. Geol.* **181**, 99–111.

Chesley J., Halliday A. N. and Scrivener R. C. (1991) Samarium–neodymium direct dating of fluorite mineralization. *Science* **252**, 949–951.

Chesley J., Halliday A. N., Kyser T. K. and Spry P. G. (1994) Direct dating of Mississippi valley-type mineralization; use of Sm–Nd in fluorite. *Econ. Geol.* **89**, 1192–1199.

Dahl P. S. (1997) A crystal-chemical basis for Pb retention and fission-track annealing systematics in U-bearing minerals, with implications for geochronology. *Earth Planet. Sci. Lett.* **150**, 277–290.

Dill H. G. and Weber B. (2010) Accessory minerals of fluorite and their implication regarding the environment of formation (Nabburg–Wölsendorf fluorite district, SE Germany), with special reference to fetid fluorite (“Stinkspat”). *Ore Geol. Rev.* **37**(2), 65–86.

Dodson M. H. (1973) Closure temperature in cooling geochronological and petrological systems. *Contrib. Mineral. Petrol.* **40**, 259–274.

Evans N. J., Wilson N., Cline J., McInnes B. I. A. and Byrne J. (2005) Fluorite (U–Th)/He thermochronology: constraints on the low temperature history of Yucca Mountain, Nevada. *Appl. Geochem.* **20**, 1099–1105.

Farley K. A. (2000) Helium diffusion from apatite: general behavior as illustrated by Durango fluorapatite. *J. Geophys. Res.* **105**, 2903–2914.

Farley K. A. (2007) He diffusion systematics in minerals: evidence from synthetic monazite and zircon structure phosphates. *Geochim. Cosmochim. Acta* **71**, 4015–4024.

Farley K. A., Wolf R. A. and Silver L. (1996) The effects of long alpha-stopping distances on (U–Th)/He ages. *Geochim. Cosmochim. Acta* **60**, 4223–4229.

Farley K. A., Reiners P. W. and Nenow V. (1999) An apparatus for high-precision helium diffusion measurements from minerals. *Anal. Chem.* **71**, 2059–2061.

Fechtig H. and Kalbitzer S. (1966) The diffusion of argon in potassium-bearing solids. In *Potassium Argon Dating* (eds. A. O. Schaeffer and J. Zähringer). Springer-Verlag, New York, pp. 68–106.

Flowers R. M., Ketcham R. A., Shuster D. L. and Farley K. A. (2009) Apatite (U–Th)/He thermochronometry using a radiation damage accumulation and annealing model. *Geochim. Cosmochim. Acta* **73**, 2347–2365.

Gautheron C., Tassan-Got L., Barbarand J. and Pagel M. (2009) Effect of alpha-damage annealing on apatite (U–Th)/He thermochronology. *Chem. Geol.* **266**, 157–170.

Gigoux M., Delpech G., Guerrot C., Pagel M., Augé T., Négrel P. and Brigaud B. (2015) Evidence for an Early Cretaceous mineralizing event above the basement/sediment unconformity in the intracratonic Paris Basin: paragenetic sequence and Sm–Nd dating of the world-class Pierre-Perthuis stratabound fluorite deposit. *Miner. Deposita* **50**, 455–463.

Guenthner W. R., Reiners P. W., Ketcham R. A., Nasdala L. and Giester G. (2013) Helium diffusion in natural zircon: radiation damage, anisotropy, and the interpretation of zircon (U–Th)/He thermochronology. *Am. J. Sci.* **313**, 145–198.

Hofstra A. H., Premo W. R., Emsbo P., Cline J. S. and Aleinikoff J. N. (2000) U–Th–Pb dating of hydrothermal minerals from Carlin-type gold deposits: results and evaluation. In *Geology and Ore Deposits 2000: The Great Basin and Beyond* (eds. J. K. Cluer, J. G. Price, E. M. Struhsacker, R. F. Hardyman and C. L. Morris), pp. 61–65.

Kazanskii S. A., Ryskin A. I., Nikiforov A. E., Zaharov Y., Ougrumov M. and Shakurov G. S. (2005) EPR spectra and crystal field of hexamer rare-earth clusters in fluorites. *Phys. Rev. B* **72**, 014127.

Kempe U. and Belyatsky B. V. (2000) Direct isotope dating of W (–Y) mineralization at Kyzyltau (Mongolian Altai): preliminary results. *Int. Geol. Rev.* **42**, 470–480.

Kempe U. and Götze J. (2002) Cathodoluminescence (CL) behaviour and crystal chemistry of apatite from rare-metal deposits. *Mineral. Mag.* **66**, 151–172.

Kempe U., Plötze M., Brachmann A. and Böttcher R. (2002) Stabilisation of divalent rare earth elements in natural fluorite. *Mineral. Petrol.* **76**, 213–234.

Kempe U., Trinkler M. and Brachmann A. (1994) Brauner Fluorit aus Sn–W-Lagerstätten – Chemismus und Farbursachen. *Beih. z. Eur. J. Mineral.*, 6.

Ketcham R. A., Guenthner W. R. and Reiners P. W. (2013) Geometric analysis of radiation damage connectivity in zircon, and its implications for helium diffusion. *Am. Mineral.* **98**, 350–360.

Lovera O. M., Richter F. M. and Harrison T. M. (1989) The ^{40}Ar/^{39}Ar thermochronometry for slowly cooled samples having a distribution of diffusion domain sizes. *J. Geophys. Res.* **94**, 17917–17935.

McDougall I. and Harrison T. M. (1988) *Geochronology and Thermochronology by the ^{40}Ar/^{39}Ar Method*. Oxford University Press, New York.

Möller P., Bau M., Dulski P. and Lüders V. (1998) REE and yttrium fractionation in fluorite and their bearing on fluorite formation. In *Proceedings of the Ninth Quadrennial IAGOD Symposium* (ed. R. D. Hagni). E. Schweizerbart'sche, Stuttgart.

Moore D. S. and Wright J. C. (1981) Laser spectroscopy of defect chemistry in CaF2:Er3+. *J. Chem. Phys.* **74**, 1626.

Nasdala L., Irmer G. and Wolf D. (1995) The degree of metamictization in zircon: a Raman spectroscopic study. *Eur. J. Mineral.* **7**, 471–478.

Nasdala L., Reiners P. W., Garver J. I., Kennedy A. K., Stern R. A., Balan E. and Wirth R. (2004) Incomplete retention of radiation damage in zircon from Sri Lanka. *Am. Mineral.* **89**, 219–231.

Nekrasov K. A. and Kupryashkin A. Ya. (2001) Recovery of the potential of interaction between helium atoms and fluorine ions using the data on interstitial diffusion and solubility of helium in fluorides of alkaline earth metals. *High Temp.* **39**, 229–234.

Nowacki W. (1938) Die Kristallstruktur des kubischen Yttrium-fluorids YF3. *Z. Kristallogr. Kristallgeom. Kristallphys. Kristallchem.* **100**, 242–250.

Pi T., Solé J. and Taran Y. (2005) (U–Th)/He dating of fluorite: application to the La Azul fluorspar deposit in the Taxco mining district, Mexico. *Miner. Deposita* **39**, 976–982.

Presser V. and Glotzbach C. (2009) Metamictization in zircon: Raman investigation following a Rietveld approach. Part II: sampling depth implication and experimental data. *J. Raman Spectrosc.* **40**, 499–508.

Reiners P. W., Farley K. A. and Hickes H. (2002) He diffusion and (U–Th)/He thermochronometry of zircon: initial results from Fish Canyon Tuff and Gold Butte. *Tectonophysics* **349**, 297–308.

Romer R. L., Förster H.-J. and Štemprok M. (2010) Age constraints for the late-Variscan magmatism in the Altenberg-Teplice Caldera (Eastern Erzgebirge/Krušné hory). *N. Jb. Miner. Abh.* **187**, 289–305.

Seifert T., Atanasova P., Gutzmer J. and Pfänder J. (2011) Mineralogy, geochemistry and age of greisen mineralization in the Li–Rb–Cs–Sn–W deposit Zinnwald, Erzgebirge, Germany. *Mineral. Mag.* **75**, 1833.

Shuster D. L. and Farley K. A. (2003) ^{4}He/^{3}He thermochronometry. *Earth Planet. Sci. Lett.* **217**, 1–17.

Shuster D. L. and Farley K. A. (2009) The influence of artificial radiation damage and thermal annealing on helium diffusion kinetics in apatite. *Geochim. Cosmochim. Acta* **73**, 183–196.

Shuster D. L., Flowers R. M. and Farley K. A. (2006a) Radiation damage and helium diffusion kinetics in apatite. *Geochim. Cosmochim. Acta* **70**, A590.

Shuster D. L., Flowers R. M. and Farley K. A. (2006b) The influence of natural radiation damage on helium diffusion kinetics in apatite. *Earth Planet. Sci. Lett.* **249**, 148–161.

Siebel W., Hann H. P., Danišík M., Shang C. K., Berthold C., Rohrmüller J., Wemmer K. and Evans N. J. (2009) Age constraints on faulting and fault reactivation: a multi-chronological approach. *Int. J. Earth Sci.* **99**, 1187–1197.

Stockli D. and Farley K. A. (2004) Empirical constraints on the titanite (U–Th)/He partial retention zone from the KTB drill hole. *Chem. Geol.* **207**, 223–236.

Tripathy-Lang A., Fox M. and Shuster D. L. (2015) Zircon ^{4}He/^{3}He thermochronometry. *Geochim. Cosmochim. Acta* **166**, 1–14.

Voigt T. (2009) The Lusatia-Krkonoše high as a late Cretaceous inversion structure: evidence from the surrounding Cretaceous basins. *Z. Geol. Wiss.* **37**, 15–39.

Wolff R., Dunkl I., Kempe U. and von Eynatten H. (2015a) The age of the latest hydrothermal overprint of tin and polymetallic deposits in the Erzgebirge, Germany: constraints from fluorite (U–Th–Sm)/He thermochronology. *Econ. Geol.* **110**, 2025–2040.

Wolff R., Dunkl I., Lange J.-M., Tonk C., Voigt T. and von Eynatten H. (2015b) Superposition of burial and hydrothermal events: post-Variscan thermal evolution of the Erzgebirge, Germany. *Terra Nova* **27**(4), 292–299.

Ziegler J. F., Ziegler M. D. and Biersack J. P. (2010) SRIM–the stopping and range of ions in matter (2010). *Nucl. Instrum. Methods Phys. Res., Sect. B* **268**, 1818–1823.

Associate editor: David L. Shuster